Anal Bioanal Chem (2014) 406:7841–7853
DOI 10.1007/s00216-014-7891-8

RESEARCH PAPER

Asymmetrical flow field-flow fractionation with multi-angle light scattering and quasi-elastic light scattering for characterization of polymersomes: comparison with classical techniques

Ugo Till · Mireille Gaucher-Delmas · Pascale Saint-Aguet · Glenn Hamon · Jean-Daniel Marty · Christophe Chassenieux · Bruno Payré · Dominique Goudounèche · Anne-Françoise Mingotaud · Frédéric Violleau

Received: 13 January 2014 / Revised: 17 April 2014 / Accepted: 13 May 2014 / Published online: 21 June 2014

Abstract Polymersomes formed from amphiphilic block copolymers, such as poly(ethyleneoxide-*b*-ε-caprolactone) (PEO-*b*-PCL) or poly(ethyleneoxide-*b*-methylmethacrylate), were characterized by asymmetrical flow field-flow fractionation coupled with quasi-elastic light scattering (QELS), multi-angle light scattering (MALS), and refractive index detection, leading to the determination of their size, shape, and molecular weight. The method was cross-examined with more classical ones, like batch dynamic and static light scattering, electron microscopy, and atomic force microscopy. The results show good complementarities between all the techniques; asymmetrical flow field-flow fractionation being the most pertinent one when the sample exhibits several different types of population.

Keywords Asymmetrical flow field-flow fractionation · Polymersomes · Self-assemblies · Shape · Molecular weight

Published in the topical collection *Field- and Flow-based Separations* with guest editors Gaetane Lespes, Catia Contado, and Bruce Gale.

Electronic supplementary material The online version of this article (doi:10.1007/s00216-014-7891-8) contains supplementary material, which is available to authorized users.

U. Till · G. Hamon · J.-D. Marty · A.-F. Mingotaud (✉)
Université de Toulouse, UPS/CNRS, IMRCP,
118 route de Narbonne, 31062 Toulouse Cedex 9, France
e-mail: afmingo@chimie.ups-tlse.fr

U. Till · M. Gaucher-Delmas · F. Violleau (✉)
Université de Toulouse, Institut National Polytechnique de Toulouse–Ecole d'Ingénieurs de Purpan, Département Sciences Agronomiques et Agroalimentaires, UPSP/DGER 115,
75 voie du TOEC, BP 57611, 31076 Toulouse Cedex 03, France
e-mail: frederic.violleau@purpan.fr

P. Saint-Aguet
Technopolym, Institut de Chimie de Toulouse,
118 route de Narbonne, 31062 Toulouse Cedex 9, France

C. Chassenieux
LUNAM Université, Université du Maine, IMMM UMR CNRS 6283, Département PCI, Avenue Olivier Messiaen,
72085 Le Mans Cedex 09, France

B. Payré · D. Goudounèche
Centre de Microscopie Electronique Appliquée à la Biologie, Faculté de Médecine Toulouse Rangueil, Université de Toulouse,
133, route de Narbonne, 31062 Toulouse cedex 4, France

Introduction

In the field of nanomedicine, the last two decades have led to the multiplication of polymeric self-assemblies used for drug delivery [1]. Potential applications span from diagnostic to the treatment of various pathologies, such as cancer, diabetes, or central nervous system diseases. These nanovectors present the strong advantage of modifying the biodistribution of the drug, which leads to an increased delivery in the tumors for example. This obviously leads to a strong decrease of the side effects which are severe in the case of chemotherapy and therefore improves the life expectancy of the patient. Several types of nanovectors are used, from the liposomes made of small surfactant molecules to polymer self-assemblies or inorganic nanocarriers such as gold nanoparticles. Historically, the first vectors used were the liposomes, but these led to fast clearance from blood circulation and exhibited poor stability. Liposomes were then modified on their surface by poly(ethyleneglycol) chains, enabling longer circulation times, which has led to the development of Doxil in USA and Europe. A further step was made by the use of polymeric self-assemblies especially thanks to the pioneering work of

Kataoka's team in Japan. A couple of polymeric micelles are thus already in the market or under clinical studies. They show a high improvement of stability compared to liposomes, but in some cases, they still have the tendency to release their cargo too early in the delivery process. This is why polymersomes, i.e., polymer self-assemblies analogous to liposomes, are increasingly studied [2–8].

Although numerous teams have examined nanovectors, only a small percentage of them fulfills the requirements for being really used. Beside the huge challenge of cancer variability, another point is their characterization. Indeed, this is of prior importance because their interaction with the living cells will depend on their chemical structure, purity, dynamical exchange with the outside environment, surface charge, and hydrophobic/hydrophilic balance. Classically, a few techniques are used, such as dynamic light scattering or electron microscopy to achieve such characterizations. The first one enables the determination of an average hydrodynamical diameter, whereas the second one allows direct visualization of the samples but is restricted to a small part of them. Lately, a few teams have begun to characterize nanovectors using these classical techniques in combination with the asymmetrical flow field-flow fractionation (AsFlFFF) technique, which has been the subject of a recent review [9]. As reported in this, "regulatory institutions such as the US Food and Drug Administration (FDA) and the European Commission have pointed out that major limitations to the real application of current nanotechnology lie in the lack of homogeneous, pure and well-characterized NPs, also because of the lack of well-assessed, robust routine methods for their quality control and characterization."

During its development, AsFlFFF has been extensively used for environmental, food, polymer, and pharmaceutical industry analyses [10–19]. Coupled with adequate detectors, this has shown its strength for the evaluation of formulations over a very wide range of sizes (from nanometer to micrometer). Very often, AsFlFFF constituted one of the rare methods enabling the analysis of samples, based on a soft fractionation technique able to maintain the state of the different objects in solution. This is particularly important when aggregates are present. Indeed, the use of other chromatographical methods such as size exclusion chromatography may lead to an evolution of the aggregates, owing to the interaction of the sample with the stationary phase. Presently, AsFlFFF is recognized as a powerful method to characterize complex macromolecules [20] or metallic nanoparticles [21–25]. The analysis of self-assemblies such as liposomes was described as early as 1993, and several studies have been published since [26, 9, 27–30]. In all of them, AsFlFFF is used to have a thorough characterization of the liposome size and size distribution. Only a few studies have used AsFlFFF not only for the first characterization of the nano-objects, but also as a tool to understand the behavior in biological media. Such an example is that of Horie [31], examining the adsorption of proteins on metallic nanoparticles by AsFlFFF. Regarding polymeric nanovectors, AsFlFFF has been described for the characterization of biopolymers, especially because for these the molecular weight distribution of the polymers is often less controlled than for synthetic systems and less reproducible between different batches of the same formulation. For instance, gelatin nanoparticles have been characterized and the quantification of grafted PEG chains reported [9, 32]. Synthetic polymeric nanoparticles have also been examined, and AsFlFFF proved again to be pertinent since it enabled, for instance, explaining different in vivo behaviors of PEG-polylactide NPs [33, 34]. A few years ago, we described the characterization of poly(ethyleneoxide-b-ε-caprolactone) micelles linked to their use in photodynamic therapy. We proved that the encapsulated photosensitizer remained in the micelles during AsFlFFF analysis and characterized the size of the vector together with the maximum drug loading [35, 36]. Recently, Miller has reported the use of AsFlFFF as a tool to assess the stability of polymeric micelles in the presence of blood serum [37]. Until now, to the best of our knowledge, no study has been published on the characterization of polymersomes by AsFlFFF.

Therefore, in this paper, we present the first comparative study of several polymersomes based on poly(ethyleneoxide-b-ε-caprolactone) (PEO-b-PCL) and poly(ethyleneoxide-b-methylmethacrylate) (PEO-b-PMMA) block copolymers by asymmetrical flow field-flow fractionation and more classical methods and examine the strength and the drawbacks of each technique.

Materials and methods

All copolymers were purchased from Polymer Source Inc. (Dorval, Montréal, Canada).

Polymersome formation by film rehydration

A 20-mg mL^{-1} polymer solution in chloroform was prepared, and the solvent was evaporated on a rotary evaporator to form a regular film which was further dried under vacuum for 4 h. The film was then rehydrated with 2 mL of Milli-Q water (filtered on a 0.2-μm filter) and heated at 65 °C for 30 min and 1 h at 65 °C under sonication. The solution was then extruded on a mini-extruding system from Avanti Polar Lipids through a polycarbonate membrane with a cutoff of 0.4 μm.

Polymersome formation by nanoprecipitation

Twenty milligrams of the polymer was dissolved in 0.4 mL of acetone. This solution was added dropwise to 5 mL of Milli-Q water (filtered on a 0.2-μm filter) under stirring over 10 min.

The solution was then further stirred for 30 min and left standing for 2 days to evaporate acetone.

Polymersome formation by dialysis

Ten milligrams of the polymer was dissolved in 2 mL of tetrahydrofuran (THF). This solution was added dropwise to 4 mL of Milli-Q water (filtered on a 0.2-μm filter) under stirring over 20 to 30 min. The solution was then dialyzed (with an 8-kDa regenerated cellulose membrane) against 600 mL of water for 1 day (and changed four times) to remove THF.

Transmission electron microscopy

TEM experiments were performed with a Hitachi HT7700 (Hitachi High-Tech, Hitachinaka, Japan) microscope (accelerating voltage of 75 kV). Small amounts of particle suspensions in water were deposited onto a discharged copper grid coated with a carbon membrane and wiped with absorbing paper. A few drops of uranyl acetate solution were deposited onto the grid for 10 s, and the grid was then dried under a lamp for at least 5 min.

Atomic force microscopy

The samples were deposited on a glass slide and left to dry. They were analyzed on a JPK NanoWizard 3 (JPK Instruments, Berlin, Germany) either in contact or tapping mode.

Simultaneous static and dynamic light scattering

Static light scattering (SLS) and dynamic light scattering (DLS) measurements were performed on an ALV CGS3 (ALV, Langen, Germany) spectrometer operating at λ= 632.8 nm. All LS data were collected at 37 °C. SLS and DLS data were recorded simultaneously for each system. Measurements were made at 6 different concentrations ranging from 0.001 to 1 mg mL^{-1} and 18 different angles (θ) ranging from 12 to 150°. The scattering vector was defined as $q=4\pi n/\lambda[\sin(\theta/2)]$, in which n is the refractive index of the solvent. The scattered intensity was measured over a period varying from 30 to 80 s to determine both the intensity autocorrelation function, $g2(t)$, from DLS and the mean scattered intensity, I, from SLS. For DLS data, the measured $g2(t)$ was related to the electric field autocorrelation function, $g1(t)$, using the Siegert relation. The resulting functions were analyzed using the REPES routine, assuming a continuous distribution of relaxation times, $A(\log(\tau))$, according to Eq. 1. The difference between the measured and calculated baselines for the DLS correlation functions was less than 0.1 %.

$$g_1(\log(t)) = \int_0^\infty \tau A(\tau)\exp\left(-\frac{t}{\tau}\right)d[\log\tau] \quad (1)$$

For most samples, the resulting distribution of relaxation times was monomodal. The relaxation times were q^2-dependent (Fig. S1, Electronic Supplementary Material), indicating that diffusive motions were probed. The apparent diffusion coefficient (D) was calculated using the relation $D=(q^2\tau)^{-1}$. The diffusion coefficient was used to calculate the hydrodynamic radius (R_H) for the relaxation mode according to the Stokes–Einstein equation.

The Rayleigh ratio R_θ for the mode of relaxation was calculated according to Eq. 2

$$R_\theta = A\frac{I_{\text{sample}}(\theta)-I_{\text{solvent}}(\theta)}{I_{\text{reference}}(\theta)}R_{\text{reference}} \quad (2)$$

in which A is the amplitude for the mode of relaxation at a given scattering angle determined by DLS (Eq. 1); I_{sample}, I_{solvent}, and $I_{\text{reference}}$ are the scattered intensities at angle θ, by the sample, solvent, and a reference liquid, respectively; and $R_{\text{reference}}$ is the Rayleigh ratio for the reference liquid. Toluene was used as the reference in our case.

The weight-average molecular weight (M_w), second virial coefficient (A_2), and radius of gyration (R_g) can be estimated according to the following:

$$\frac{Kc}{R_\theta} = \frac{1}{\overline{M_w}}\left(1+\frac{q^2R_g^2}{3}\right)+2A_2c \quad (3)$$

in which c is the solution concentration and K is a constant, given by Eq. 4.

$$K = \frac{4\pi^2 n_{\text{ref}}^2 (dn/dc)^2}{\lambda^4 N_A} \quad (4)$$

In Eq. 4, n_{ref} is the refractive index of the reference liquid, dn/dc is the refractive index increment of the polymer, and N_A is Avogadro's number. The refractive index increments dn/dc of the polymersomes in water were measured with a PSS dndc-2010 instrument at 620 nm at 37 °C. For PEO-PCL 5–32, due to the turbidity of the solutions, the dn/dc value was evaluated from AsFlFFF fractograms, assuming 90–100 % mass recovery.

Polymer	dn/dc (mL g^{-1})
PEO-PCL 2–4.8	n.d.
PEO-PCL 2–7	0.152
PEO-PCL 5–11	0.149
PEO-PCL 5–32	Determined from RI data coupled with AsFlFFF at ca. 0.125
PEO-PMMA 1.4–5.6	0.156

Apart from PEO-PMMA 1.4–5.6, Kc/R_θ was independent of c (Figs. S2 and S3, Supporting Information); therefore, Kc/R_θ values were plotted vs q^2 to determine M_w and R_g. The reported error for all light scattering results was 10 % of the average value.

In order to assess the shape of the self-assemblies, $R_\theta c/K$ was plotted vs q and compared to the theoretical ones calculated from the following equations expressing the form factor $P(q)$.

Shape	Form factor $P(q)$*
Sphere	$9A\left(\frac{\sin qr - qr\cos qr}{(qr)^3}\right)^2$
Vesicle	$A\frac{\sin^2(qr)}{q^2r^2}$

*A is an adjusting parameter, and r is the size of the object.

Small-angle neutron scattering experiments

For small-angle neutron scattering (SANS), PEO-PCL 5–11 polymersomes were prepared following the film rehydration/extrusion method using D_2O instead of regular water. SANS experiments were performed with the PACE spectrometer at the Orphée reactor (LLB, Saclay). Polymer solutions in D_2O solvent were put inside quartz cells of 2 mm path length and measured at 20 °C ([polymer]=1 % *w*/*v*). Two spectrometer configurations were used: a neutron wavelength (λ) of 6 Å with a sample-to-detector distance of 3 m and a wavelength of 13 Å with a distance of 4.7 m. The scattering vector range thus reached was $0.0032 < q$ (Å^{-1}) < 0.12. Scattering intensities have been normalized by the incoherent signal delivered by a 1-mm gap water sample in order to account for the efficiency of the detector [38]. Absolute values of the scattering intensity $I(q)$ in cm^{-1} were obtained from the direct determination of the number of neutrons in the incident beam and the detector cell solid angle [39]. No background has been subtracted to the sample scattering; thus, a flat incoherent signal has been observed at high q values. Data treatment was done with the PAsiDUR software at the Laboratoire Léon Brillouin.

Asymmetrical flow field-flow fractionation

The asymmetrical flow field-flow fractionation instrument was an Eclipse 2 System (Wyatt Technology Europe, Dernbach, Germany). The AsFlFFF channel designed with a 190-μm-thick Mylar spacer had a trapezoidal shape with a length of 17.3 cm, an initial breadth of 1.65 cm, and a final breadth of 0.30 cm. The accumulation wall was an ultrafiltration membrane of regenerated cellulose with a 5-kDa cutoff (Wyatt Technology Europe, Dernbach, Germany). An Agilent 1100 Series Isocratic Pump (Agilent Technologies, Waldbronn, Germany) with an in-line vacuum degasser and an Agilent 1100 Autosampler delivered the carrier flow and handled sample injection into the AsFlFFF channel. A 0.1-μm in-line filter (VVLP, Millipore, Germany) was installed between the pump and the AsFlFFF channel. The products were detected with 18 angles multi-angle light scattering (MALS) DAWN-HELEOS II (Wyatt Technology, Santa Barbara, CA, USA), an Optilab Rex Refractometer (Wyatt Technology, Santa Barbara, CA, USA), and a UV detector Agilent 1100 (λ=214 or 412 nm). The MALS detectors were normalized with bovine serum albumin (BSA). Calibration of scattering intensity was performed with HPLC-grade filtered toluene. Water, which was filtered with 0.02 % sodium azide before use (vacuum filtration system using Gelman filters of 0.1 μm), was used as an eluent.

During focusing, the cross flow was fixed at 0.5 mL min^{-1}. After 1 min, 10 to 60 μL of sample were injected at 0.2 mL min^{-1} for 2 min. After injection, 1 min of focus was maintained before the elution started.

In elution mode for PEO-PCL nanoparticles, the cross-flow rate was fixed to 0.4 mL min^{-1} for 10 min. For PEO-PMMA nanoparticles, the cross-flow rate was fixed to 0.2 mL min^{-1} for 10 min. For PEO-PCL 2000–4800, in order to observe the three populations, the cross-flow rate was primarily set to 0.5 mL min^{-1}. After the cross-flow rate decreased linearly for 10 min, elution followed at 0.15 mL min^{-1} for 15 min. In all the cases, cross flow was then stopped in order to eliminate all particles present in the AsFlFFF system.

Results and discussion

The polymers selected for this study are presented in Scheme 1. Two types have been chosen. The first one is poly(ethyleneoxide-b-ε-caprolactone) (PEO-b-PCL) for its high relevancy related to application in drug delivery, owing to the presence of polyethyleneglycol block leading to stealth in the bloodstream and that of poly(ε-caprolactone) being a

Scheme 1 Polymers used

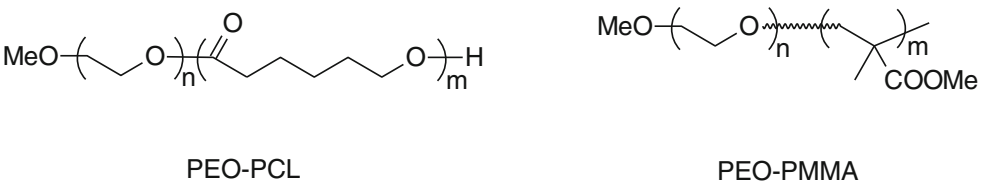

Table 1 Formation of polymersomes

Polymer	M_n of PEO block (g mol^{-1})	M_n of hydrophobic block (g mol^{-1})	$f_{hydrophilic}$ [a] (%)	Preparation method
PEO-PCL 2–4.8	2,000	4,800	29.4	Film rehydration
PEO-PCL 2–7	2,000	7,000	22.2	Film rehydration
PEO-PCL 5–11	5,000	11,000	31.2	Film rehydration
PEO-PCL 5–32	5,000	32,000	13.5	Dialysis
PEO-PMMA 1.4–5.6	1,400	5,600	20.0	Nanoprecipitation

[a] Weight fraction of hydrophilic part

degradable polyester already approved by the FDA for medical applications. In this family, several molecular weights were examined, in order to obtain polymersomes with various sizes. They were chosen so as to have a change in the hydrophilic/hydrophobic balance based on the suggested rule that polymersomes should be obtained with a preferable hydrophilic mass fraction close to 35 % [40]. The other type of polymer that was tested is poly(ethyleneoxide-b-methylmethacrylate) (PEO-b-PMMA) in order to assess the influence of the chemical structure on the analyses. Depending on the polymer and the molecular weights, different methods of preparation were used. The first one is based on liposome formation techniques and uses a rehydration of the polymer film followed by sonication and extrusion. For PEO-PCL 5–32 (Table 1), this method was shown to lead to poorly stable nano-objects and was therefore not further used. An alternative was preferred following a procedure described by Sachl et al. [41, 42]. In this case, a solution of the polymer is prepared in a good solvent and added to a large volume of water followed by dialysis to eliminate the organic solvent. Finally, in the case of PEO-PMMA 2–2.6, the extrusion proved to be impossible, the objects being unable to pass through the filter. This was attributed to the strong mechanical strength of the PMMA core (glass transition temperature at 105 °C) compared to poly(ε-caprolactone) (glass transition temperature at −60 °C). In this case, a method of nanoprecipitation was processed with acetone as cosolvent.

Electron and atomic microscopies

For these techniques, the sample has to be dried and is observed only over a narrow scale range. Typical images for the systems presented here are given in Figs. 1 and 2. In TEM, two types of images could be described, showing either spherical/ovoid or elongated objects. The spherical systems were analyzed to extract their distribution, and this showed rather polydisperse populations. In AFM, the same comment also holds although the round shape for the nano-objects was in some instance more difficult to assess. Typical magnitude ranges for the size of the self-assemblies are reported in

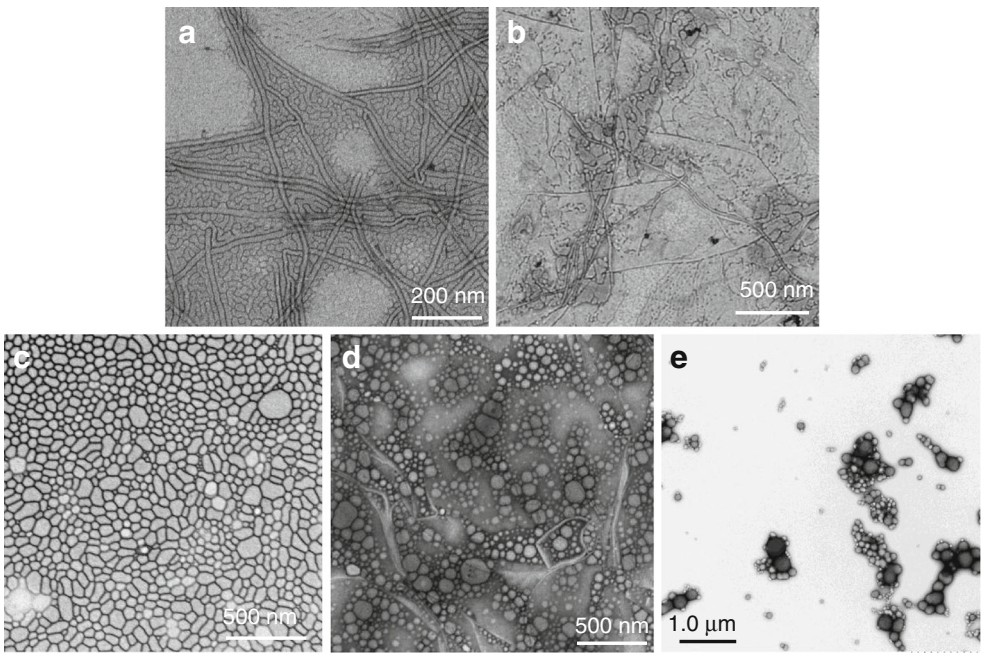

Fig. 1 TEM micrographs of polymer self-assemblies. **A** PEO-PCL 2–4.8; **B** PEO-PCL 2–7; **C** PEO-PCL 5–11; **D** PEO-PCL 5–32; **E** PEO-PMMA 1.4–5.6

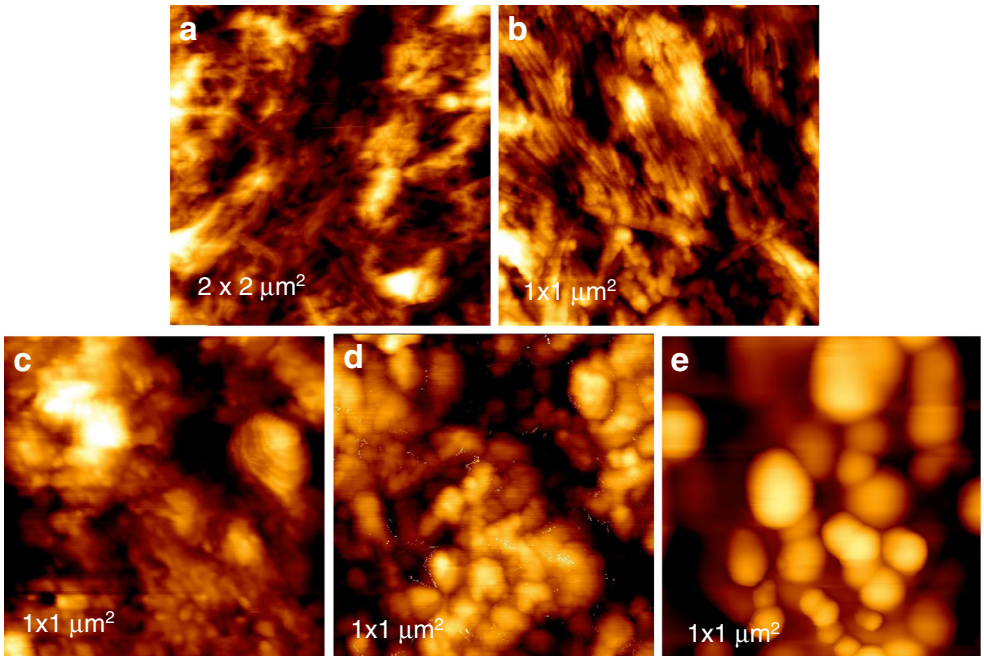

Fig. 2 Height AFM images of polymer self-assemblies. **A** PEO-PCL 2–4.8; **B** PEO-PCL 2–7; **C** PEO-PCL 5–11; **D**. PEO-PCL 5–32; **E** PEO-PMMA 1.4–5.6

Table 2. Depending on the polymer, self-assemblies as small as 20 nm can be observed up to larger ones of several hundreds of nanometers. Although these techniques give valuable information on the sample, they suffer from the uncertainty of the drying and staining process, implying that the images are not necessarily representative of the real objects in the solution. For this, in some instances, cryo-TEM or cryo-SEM can be carried out but small and poorly contrasted objects are still often difficult to observe.

Static and dynamic light scattering

By opposition to the former techniques, batch static or dynamic light scattering enables an analysis of the objects in solution. Light scattering is indeed one of the most used methods to characterize polymer self-assemblies, partly because of its wide availability and the apparent simplicity of obtaining results. Most usually, dynamic light scattering (DLS) is routinely used to determine the size of the self-assemblies in solution. As described in the "Materials and methods" section, the registered parameter is the fluctuation with time of the light scattered by the nano-objects in solution upon irradiation of the sample. From these fluctuations, the diffusion coefficient of the scattering objects is measured and their hydrodynamical radius R_H computed from the Stokes–Einstein equation. Using the value of the time-average scattered intensity instead of its fluctuation, static light scattering (SLS) is performed and enables the determination of molecular weight (leading to the aggregation number of the self-assemblies) and that of the radius of gyration R_g. The knowledge of both R_H and R_g is interesting from an analytical standpoint because the ratio R_g/R_H provides information regarding the morphology of the self-assembly. For homogeneous spheres, this is expected to be 0.774; for empty spheres

Table 2 Characteristics of the self-assemblies derived from TEM and AFM observations

Polymer	TEM observations	AFM observations
PEO-PCL 2–4.8	Elongated objects 20 nm wide, several hundred nm long+smaller structures 20–100 nm	No clearly defined nano-objects
PEO-PCL 2–7	No clearly defined objects, some elongated structures	Worm-like objects, several hundred nm long
PEO-PCL 5–11	Well-defined ovoid objects, diameter range 50–200 nm, 62.6±28.1 nm	Aggregates of spherical objects, size range 20–50 nm
PEO-PCL 5–32	Clear, well-defined spheres, diameter range 20–100 nm, 39.9±15.9 nm	Aggregates of spherical objects, size range 20–80 nm
PEO-PMMA 1.4–5.6	Clear, well-defined spheres, diameter range 20–300 nm, aggregates 121±77 nm for unimers	Aggregates of spheres clearly visible, size range 60–200 nm

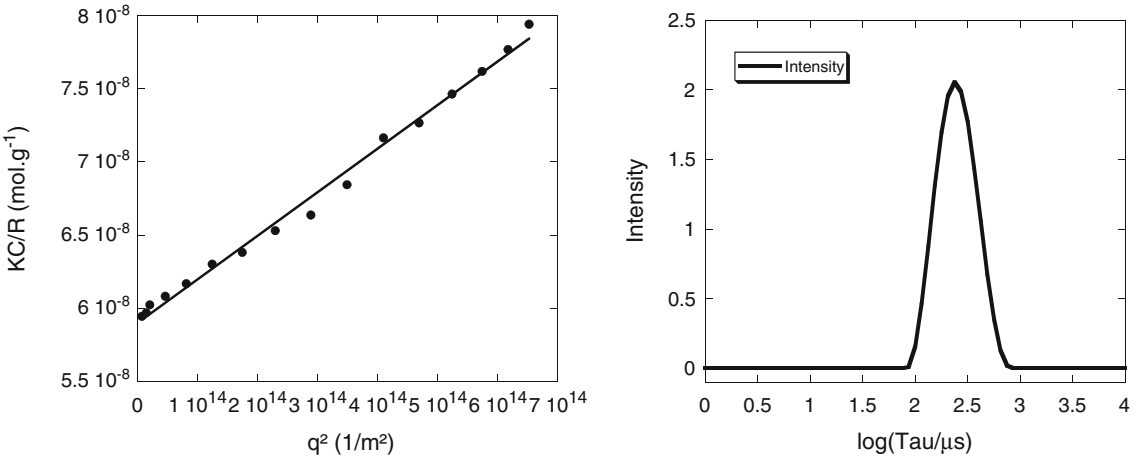

Fig. 3 Typical SLS (*left*) and DLS (*right*) graphs

such as polymersomes, the value should approach 1; and for elongated objects, this value may increase up to 2 depending on the anisotropy. Such information is important for medical applications, since an increasing number of studies show that the shape of the nanovectors will determine their fate in vivo and will therefore influence the drug delivery [43, 44]. All the systems presented here were thus analyzed by both SLS and DLS. Typical results from SLS and DLS are plotted in Fig. 3. The molecular weight of the self-assembly can be derived from the intercept of Kc/R_θ vs q^2, whereas the value of the radius of gyration is determined from the slope. The values which have been measured are reported in Table 3.

For the polymers of Table 3, the observed objects exhibited diameters ranging from 80 to 160 nm and the shape was spherical, except for PEO-PCL 2–7 (*vide infra*). PEO-PMMA self-assemblies are demonstrated to be polymersomes whereas the R_g/R_H ratio for PEO-PCL 5–32 self-assemblies lies in between that of vesicles (1.0) and that of homogeneous spheres (0.774). In order to assess in more detail their shape, experimental data were fitted with the form factor (experimental part) of vesicles and spheres for all spherical systems. The results are reported in Fig. 4 for PEO-PMMA 1.4–5.6 and Fig. S4 for PEO-PCL 5–11 and PEO-PCL 5–32. For both PEO-PCL 5–11 and PEO-PMMA 1.4–5.6, the experimental data are better adjusted with the vesicle model than with the sphere one, in agreement with the observed R_g/R_H value. For PEO-PCL 5–32, both sphere and vesicle fits are possible, and further characterizations are therefore needed to discriminate these two architectures.

The size found for PEO-PMMA 1.4–5.6 is close to that measured with TEM and AFM. However, in TEM, a clear wide distribution was visible, since objects as small as 20 nm appeared on the images. Another point worth mentioning is the fact that it was possible to analyze the influence of dilution on the aggregates for PEO-PMMA 1.4–5.6. Indeed, a strong evolution of Kc/R_θ with concentration was observed, showing the gradual disappearance of aggregates in favor of unimeric polymersomes (Fig. S3).

PEO-PCL 2–4.8 is not reported in Table 3, since it exhibited a multimodal distribution of relaxation times revealing several populations of nano-objects.

The last polymer, PEO-PCL 2–7, exhibited a single population, the shape of which was found to be cylindrical, since R_θ/Kc exhibited a power law dependence: $R_\theta/Kc \sim 1/q$ (Fig. 5). However, for this, the Guinier regime was not attained, and therefore, an estimation of the cylinder dimensions was not possible.

As already said, compared to TEM and AFM, SLS and DLS give an analysis of the whole sample in solution which may enable measuring the real size of the objects, as long as the equations used to evaluate the size are still pertinent and the polydispersity is not too high. As shown for PEO-PCL 2–7, one has to be very cautious in using those since the observed object might not be spherical. Cryo-TEM and

Table 3 Characteristics of the spherical self-assemblies measured by DLS and SLS

Polymer	R_g (nm)	R_H (nm)	R_g/R_H	M_w (10^6 g mol^{-1})	N_{agg}[a]
PEO-PCL 5–11	80.6	72.8	1.11	192.0	12,000
PEO-PCL 5–32	41.5	48.9	0.85	17.4	465
PEO-PMMA 1.4–5.6	79.6	73.6	1.08	4.3	614
PEO-PCL 2–7	n.d.	105.4	–	207.5	23,000

[a] Number of aggregations determined from $M_{w\ polymersome}/M_{polymer}$

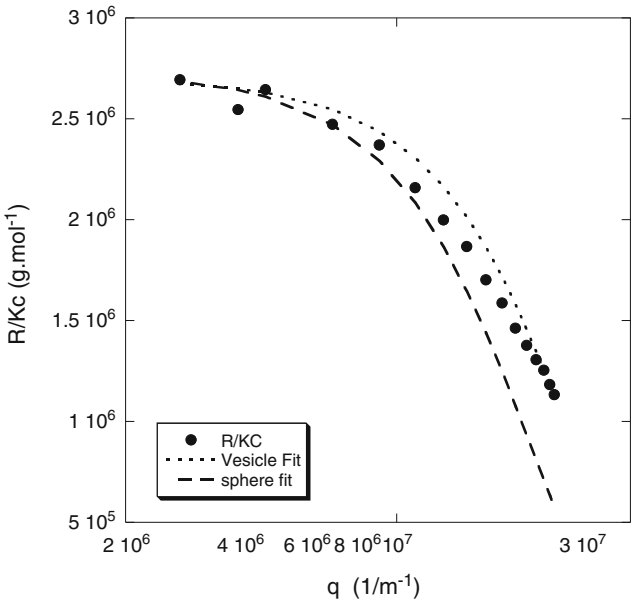

Fig. 4 Shape factor of PEO-PMMA 1.4–5.6 self-assemblies

AFM performed in solution may also give access to the real size of the objects but still give only a partial overview of the sample. Furthermore, the analysis of PEO-PCL 2–4.8 has shown that batch methods may not be adequate when several populations are present. A fine analysis of the SLS and DLS results might enable a corrected calculation when a small percent of only another population is present, but when the ratio is high or when more than two are present, then it would be erroneous to try to analyze such a sample by batch SLS or DLS.

Small-angle neutron scattering

Light scattering experiments indicated a highly probable polymersome structure. In order to have further proof, small-angle neutron scattering was carried out on PEO-PCL 5–11 self-assemblies obtained with hydrogenated polymers in D_2O. The SANS curve (Fig. 6) exhibited a huge decrease (q^{-4} decay) at large q values (q>0.01 Å^{-1}) which corresponds to the POROD's domain. At low q, it flattens, as expected for the typical q^{-2} dependence characteristic of large-vesicle flat membranes [45]. In this region, the form factor becomes proportional to $\exp(-q^2d^2/12)/q^2$ where d is the membrane thickness. Kratky–Porod representation $\ln(q^2I(q))$ vs q^2 in the q range ($1/R<q<1/d$, i.e., 0.001 Å^{-1}<q<0.01 Å^{-1}) allowed gaining access to the d value which is evaluated around 10± 4 nm. The membrane thickness was further confirmed thanks to the small bump observed at q=0.09 Å^{-1} characteristic of this thickness. This value was in good agreement with the ones observed for other families of polymersome [46, 47]. This value could be mainly ascribed to the contribution of the PCL block, the contrast of the latter being higher than that of the hydrated PEO block in D_2O [47]. The large size of those objects (see SLS and DLS measurements where R_g values around 81 nm were observed) does not allow reaching the Guinier domain (q<0.001 nm^{-1}) and using the Guinier approximation to evaluate R_g values.

Asymmetrical flow field-flow fractionation

In a first step, the elution program had to be established. For this, the recovery was first evaluated on PEO-PCL 5–11 by injecting different quantities of polymersomes with no cross flow. In these conditions, 100 % of injected quantity is recovered. As the peak area detected by refractometry is proportional to the injected quantity, a calibration curve (Fig. 7) can

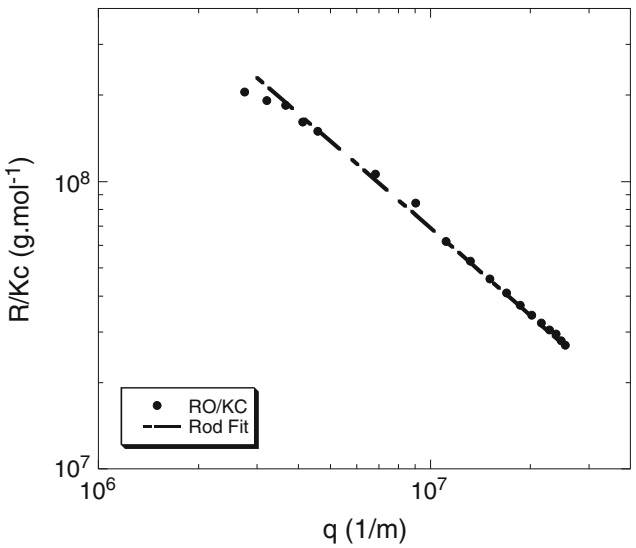

Fig. 5 SLS results for PEO-PCL 2–7

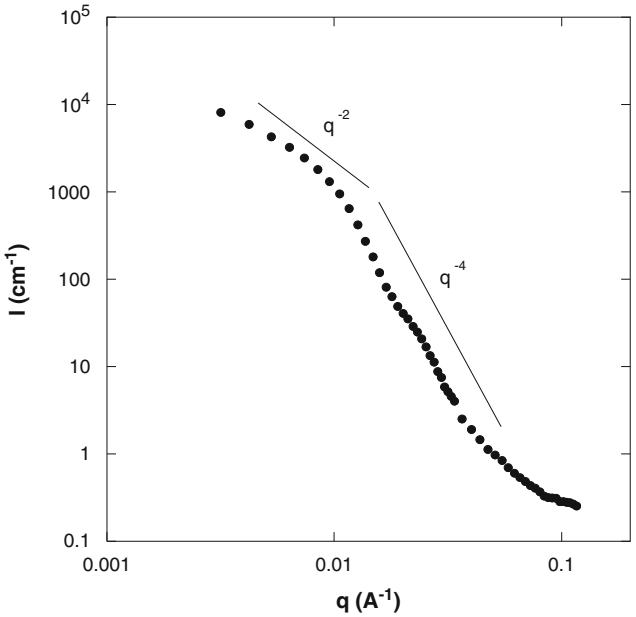

Fig. 6 SANS curve of PEO-PCL 5–11 solutions (1 wt%) in D_2O

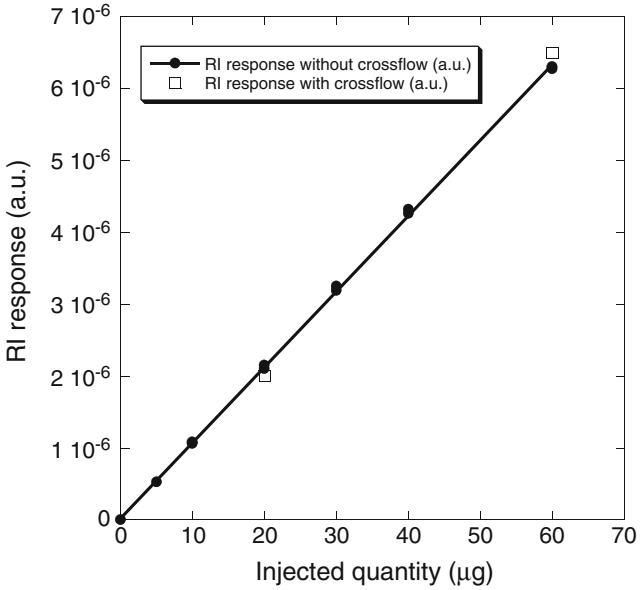

Fig. 7 Recovery percentage of PEO-PCL 5–11

be drawn. When a cross flow is applied, the recovery mass determined with the RI peak area is compared to the injected mass. The results presented in Fig. 7 show that a 98.7±4.6 % mass recovery is obtained by applying a cross flow of 0.5 mL min^{-1} after injection of 20 and 60 µg of polymersome.

After this step, elution profiles as a function of the cross flow were examined to determine the best elution program. Typical examples are reported in Fig. 8 for PEO-PCL 5–11. The sought optimal conditions should lead to a good separation of the product from the peak system inherent to this

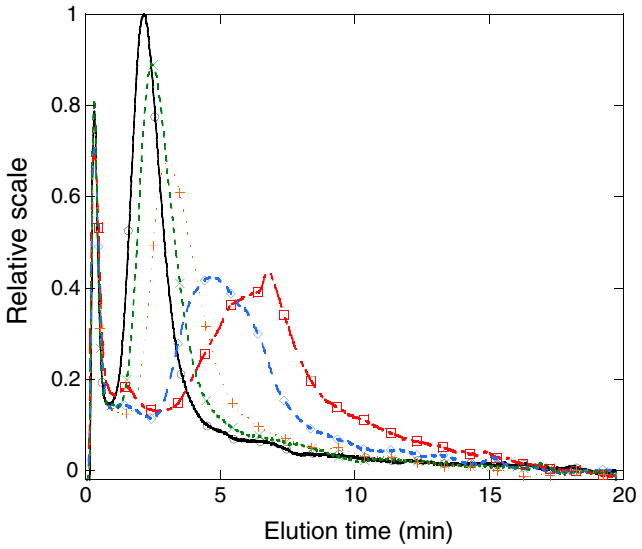

Fig. 8 Elution profiles of PEO-PCL 5–11 polymersomes at Vc= 0.9 mL min^{-1} at various cross flows (*black*: Vx=0.3 mL min^{-1}, *green*: Vx=0.4 mL min^{-1}, *orange*: Vx=0.5 mL min^{-1}, *blue*: Vx=0.7 mL min^{-1}, *red*: Vx=0.9 mL min^{-1})

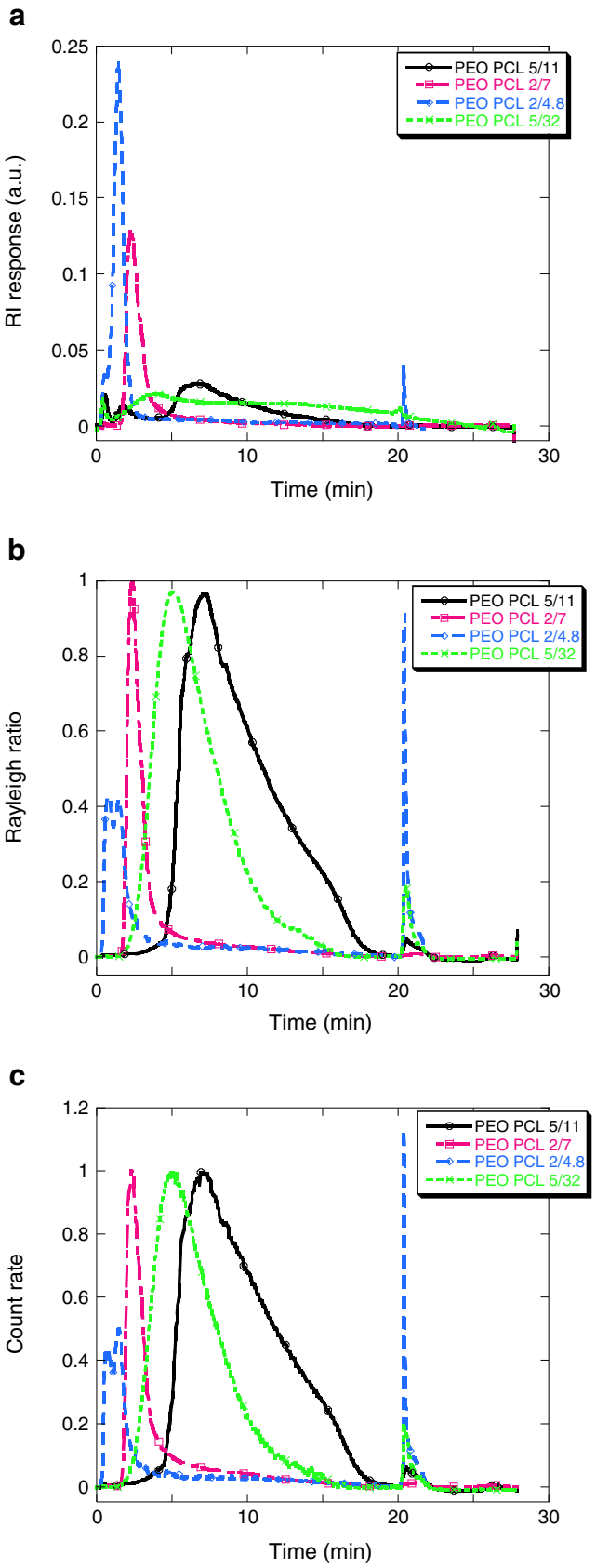

Fig. 9 AsFlFFF fractograms of PEO-PCL polymersomes (Vc= 0.9 mL min^{-1}; Vx=0.4 mL min^{-1}). **A** RI signal. **B** SLS signal. **C** QELS signal

Table 4 AsFlFFF analysis

Polymer	R_{gw} (nm)	R_{Hw} (nm)	R_g/R_H[a]	M_n (g mol^{-1})	M_w (g mol^{-1})	N_{agg}	I_p
PEO-PCL 2–4.8	40/159/154	40/135/230	n.d.	2,300,000–570,000,000	2,200,000–590,000,000	340–84,000	n.d.
PEO-PCL 2–7	112.0	68.0	1.65	130,000,000	140,000,000	15,000	1.02
PEO-PCL 5–11	143.7	66.0	2.18	1,050,000,000	1,450,000,000	65,000	1.38
PEO-PCL 5–32	46.0	60.5	0.76	31,000,000	72,000,000	820	2.32
PEO-PMMA 1.4–5.6	180.0	284.0	0.63	330,000,000	560,000,000	47,000	1.70

[a] Obtained from weight-average values for R_g and R_H

technique (coming from the beginning of elution in the analysis program) while avoiding too much widening of the object peak. This was achieved here with a cross flow of 0.4 mL min^{-1}, which was therefore chosen as the cross flow for the other analyses.

Once the elution conditions were chosen, PEO-PCL polymersomes were characterized following the same procedure. Figure 9 displays accordingly the obtained fractograms, and the characteristics of the self-assemblies in terms of molar mass, aggregation number, and sizes are given in Table 4. Except for PEO-PMMA, the values for N_{agg} are of the same order as those measured by batch SLS/DLS. For PEO-PMMA, the discrepancy comes from the presence of aggregates as discussed earlier whose contributions have been discarded during the dilution and processing of the experimental data in batch LS. For PEO-PCL 2–7, the values found for R_g and R_H are on the same order. For PEO-PCL 5–11, the obtained size is of the same order but there is a discrepancy on the R_g value leading to a much higher R_g/R_H ratio determined by AsFlFFF. This might be the consequence of shearing the objects during elution. Finally, PEO-PCL 5–32 gave similar results by both batch analysis and AsFlFFF. It is, however, noteworthy that the fractogram of this last system could possibly be composed of several populations according to the shape of the peak although elution only showed a single one. Comparing the shape of the peaks, the PEO-PCL 2–7 system clearly was the best defined one, with PEO-PCL 5–11 and 5–32 appearing as very wide peaks. This can be compared with TEM images where these systems clearly appeared as polydisperse, but this result differed from that obtained from DLS where PEO-PCL 2–7 had the highest polydispersity index (supplementary information). This discrepancy might be attributed to DLS processing assuming spherical scattering objects.

For PEO-PCL 2–4.8, studied conditions (Vc= 0.9 mL min^{-1}; Vx=0.4 mL min^{-1}) were not suited. Actually, even though part of the sample was fractionated, a significant quantity was flushed when the cross flow was stopped after 20 min of elution. Therefore, a specific analysis method was developed for the fractionation of this sample using a cross flow linear decay gradient: Vx linear decay from 0.5 to 0.15 mL min^{-1} in 5 min and Vx=0.15 mL min^{-1} during 15 min.

The corresponding fractograms are shown in Fig. 10.

The PEO-PCL 2–4.8 system exhibited at least three different populations, the hydrodynamical diameter of which can be estimated from quasi-elastic light scattering (QELS) data varying between 40 and 230 nm. This is consistent with TEM images where both elongated objects as well as spherical ones were observed, but it is different from polydispersity values obtained from batch DLS (see supplementary information), where this system presented erratic polydispersity indexes (PDIs), sometimes as low as 0.07.

Finally, PEO-PMMA 1.4–5.6 objects were also analyzed by AsFlFFF, using a different 0.2 mL min^{-1} cross flow, in order to have a full overview of the system. The fractogram showed a single population having a dissymmetrical peak (Fig. 11). The solutions had to be diluted in order to avoid saturation of the QELS and LS detectors. The dissymmetry of the peak still remained for the diluted solution indicating a

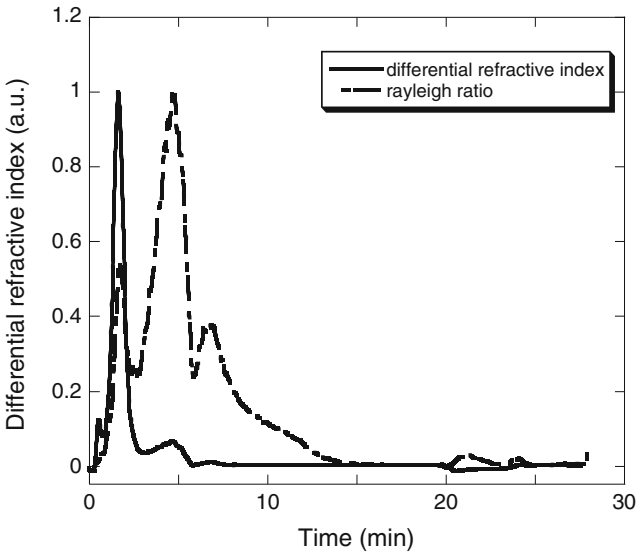

Fig. 10 AsFlFFF fractogram of PEO-PCL 2–4.8 polymersomes (Vx linear decay from 0.5 to 0.15 mL min^{-1} in 5 min; Vx=0.15 mL min^{-1} during 15 min)

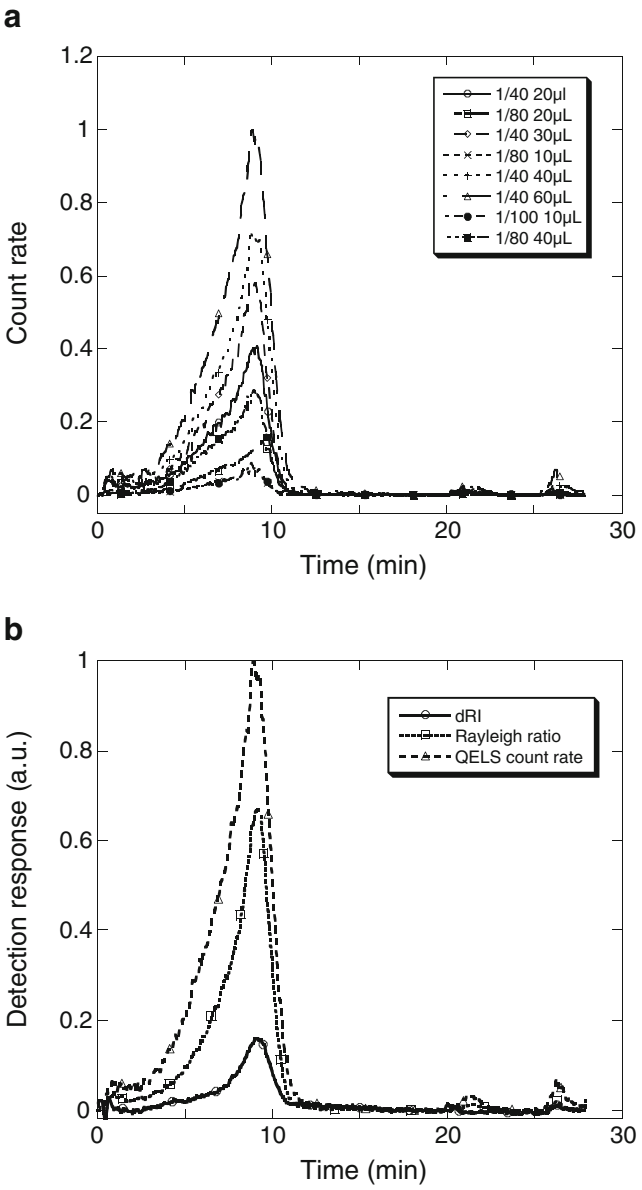

Fig. 11 AsFlFFF analysis of PEO-PMMA 1.4–5.6 polymersomes (Vc= 0.9 mL min^{-1}; Vx=0.2 mL min^{-1}). **A** QELS detection, **B** triple detection

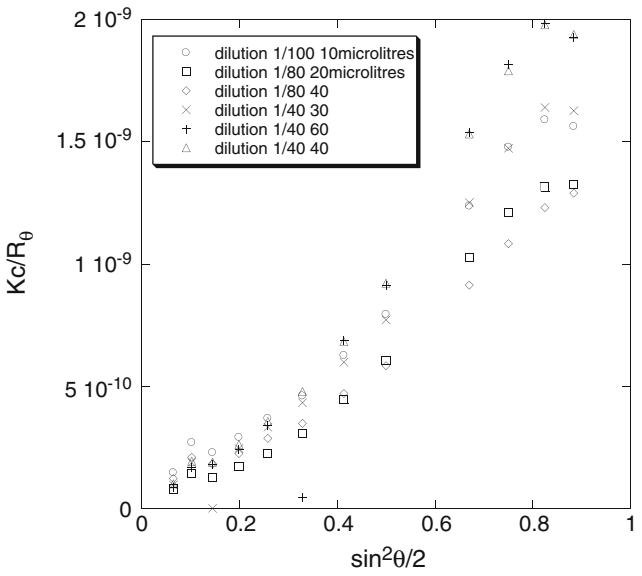

Fig. 12 Kc/R_θ measured from AsFlFFF for PEO-PMMA 1.4–5.6 polymersomes

polydisperse solution rather than overloading. The observed Kc/R_θ at each angle and injection condition did not vary (Fig. 12), meaning that in these conditions, the presence of aggregates was avoided.

At this point, it is noteworthy to have a closer analysis of the method to assess the polydispersity of self-assemblies. Table 5 presents an overview of the different techniques used in this study. For TEM analysis, the polydispersity can be evaluated from the ratio between the standard deviation and the measured value of the size. This enables a comparison between the samples, showing that PEO-PCL 5–11 and PEO-PCL 5–32 exhibit a close behavior, whereas PEO-PMMA is markedly more polydisperse. AsFlFFF experiments give two different details. First, using the same elution method, the peak profile comparison gives rapid information about the difference in the number of population, size, and size dispersion between each self-assembly. Apart from PEO-PCL 2–4.8 exhibiting several distinct populations, PEO-PCL 5–11 and PEO-PCL 5–32 are once again observed to behave similarly, whereas PEO-PCL 2–7 has a very short elution duration. Regarding the polydispersity index determined from AsFlFFF in terms of M_w/M_n, approximately the same conclusion can be drawn, but PEO-PCL 5–32 appears more disperse. However, the value of Ip for PEO-PMMA is found in between that of PEO-PCL 5–11 and PEO-PCL 5–32, which is different from the results found in TEM.

As for light scattering experiments, PDIs evaluated from the deviation from a monomodal exponential are given; they were obtained with a Malvern instrument (see Electronic Supplementary Material). These give close results compared to TEM, with PEO-PCL 5–32 being the best defined followed by PEO-PCL 5–11 and PEO-PMMA. On this measurement, it is important to mention that PEO-PCL 2–4.8 gave erratic results for PDI, ranging between 0.07 and 0.43, depending on the batch. This clearly shows that one should not use a single measurement of such solution to assess the polydispersity of the system.

Finally, PDI was also calculated on the ALV system, enabling simultaneous SLS and DLS experiments. For this, the PDI corresponds to the square of the ratio standard deviation/mean value of R_H for different solutions with different concentrations and angles. This is therefore different from PDIs evaluated on Malvern's instrument and provides information on the repeatability of the measurement itself more than the presence of several populations in the solution.

Table 5 Overview of polydispersity determination techniques

Polymer	TEM analysis results[a]	PDI ALV[b]	PDI Malvern[c]	Elution duration AsFlFFF (min)	I_p (AsFlFFF)
PEO-PCL 2–4.8	–	n.d.	0.07–0.43	–	–
PEO-PCL 2–7	–	n.d.	0.22	4	1.02
PEO-PCL 5–11	62.6±28.1 nm (0.19)	10^{-4}	0.17	13	1.38
PEO-PCL 5–32	39.9±15.9 nm (0.16)	$4\ 10^{-4}$	0.10	13	2.32
PEO-PMMA 1.4–5.6	121±77 nm for unimers (0.41)	$2.5\ 10^{-3}$	0.23	–	1.7

[a] The value in brackets corresponds to the ratio $(SD/size)^2$

[b] Calculated from SD^2 /(mean value)^2 over different concentrations

[c] Calculated from deviation from cumulant fit

From a general standpoint, this analysis enables different conclusions to be drawn. If the same trend can sometimes be found by several techniques, one should be very cautious and not limit the analysis to only one. PDIs provided by DLS (cumulant deviation) should also be taken with great care, since in this example the best defined PEO-PCL 5–32 in DLS is found to be the widest in AsFlFFF for Ip. However, the possible change of shape during elution might induce errors in the determination of molar mass and therefore in that of Ip.

Conclusion

In previous studies, we showed the performance of the AsFlFFF–MALS–QELS–RI technique for the characterization of poly(ethyleneoxide-b-ε-caprolactone) micelles. The work presented here confirmed the pertinence of this technique for the characterization of other self-assemblies like polymersomes.

Fractogram profiles of samples obtained with AsFlFFF are very informative about the composition difference between several samples and give first information about differences in size between each sample. The association of AsFlFFF with light scattering detectors gives complementary information to batch dynamic and static light scattering, electron microscopy, and atomic force microscopy experiments. The AsFlFFF–MALS–QELS–RI technique is very relevant when the samples are very complex, like samples with several different types of populations. Optimization of the AsFlFFF fractionating conditions like flow rate is carried out to increase the quality of light scattering data in order to obtain stronger information on the shape of the sample.

Acknowledgments The authors wish to thank the French ANR (ANR COPOPDT), PRES Toulouse and Midi-Pyrénées Region for funding and PhD grant for U. Till. EU (FEDER-35477: Nano-objets pour la biotechnologie) is greatly acknowledged for financial support (AFM instrument). LLB is thanked for beam time access and Annie Brûlet for fruitful discussion.

References

1. Riehemann K, Schneider SW, Luger TA, Godin B, Ferrari M, Fuchs H (2009) Nanomedicine—challenge and perspectives. Angew Chem Int Ed 48(5):872–897
2. Discher DE, Ortiz V, Srinivas G, Klein ML, Kim Y, Christian D, Cai S, Photos P, Ahmed F (2007) Emerging applications of polymersomes in delivery: from molecular dynamics to shrinkage of tumors. Prog Polym Sci 32:838–857
3. Le Meins J-F, Sandre O, Lecommandoux S (2011) Recent trends in the tuning of polymersomes' membrane. Eur Phys J E 34(2):14
4. Lee JS, Feijen J (2012) Polymersomes for drug delivery: design, formation and characterization. J Control Release 161(2):473–483
5. Letchford K, Burt H (2007) A review of the formation and classification of amphiphilic block copolymer nanoparticulate structures: micelles, nanospheres, nanocapsules and polymersomes. Eur J Pharm Biopharm 65(3):259–269
6. LoPresti C, Lomas H, Massignani M, Smart T, Battaglia G (2009) Polymersomes: nature inspired nanometer sized compartments. J Mater Chem 19(22):3576–3590
7. Meng F, Zhong Z (2011) Polymersomes spanning from nano- to microscales: advanced vehicles for controlled drug delivery and robust vesicles for virus and cell mimicking. J Phys Chem Lett 2(13):1533–1539
8. Tanner P, Baumann P, Enea R, Onaca O, Palivan C, Meier W (2011) Polymeric vesicles: from drug carriers to nanoreactors and artificial organelles. Acc Chem Res 44(10):1039–1049
9. Zattoni A, Roda B, Borghi F, Marassi V, Reschiglian P (2013) Flow field flow fractionation for the analysis of nanoparticles used in drug delivery. J Pharm Biomed Anal under press. doi:10.1016/j.jpba.2013.08.018
10. Bria C, Violleau F, Williams SKR (2013) Field-flow fractionation for biological, natural, and synthetic polymers: recent advances and trends. Lc Gc Asia Pac 16(4):8–16
11. Nilsson L (2013) Separation and characterization of food macromolecules using field-flow fractionation: a review. Food Hydrocoll 30(1):1–11
12. von der Kammer F, Legros S, Larsen EH, Loeschner K, Hofmann T (2011) Separation and characterization of nanoparticles in complex food and environmental samples by field-flow fractionation. Trends Anal Chem 30(3):425–436
13. Baalousha M, Stolpe B, Lead JR (2011) Flow field-flow fractionation for the analysis and characterization of natural colloids and manufactured nanoparticles in environmental systems: a critical review. J Chromatogr A 1218(27):4078–4103
14. Yohannes G, Jussila M, Hartonen K, Riekkola ML (2011) Asymmetrical flow field-flow fractionation technique for separation and characterization of biopolymers and bioparticles. J Chromatogr A 1218(27):4104–4116

15. Qureshi RN, Kok WT (2011) Application of flow field-flow fractionation for the characterization of macromolecules of biological interest: a review. Anal Bioanal Chem 399(4):1401–1411
16. Rambaldi DC, Reschiglian P, Zattoni A (2011) Flow field-flow fractionation: recent trends in protein analysis. Anal Bioanal Chem 399(4):1439–1447
17. Roda B, Zattoni A, Reschiglian P, Moon MH, Mirasoli M, Michelini E, Roda A (2009) Field-flow fractionation in bioanalysis: a review of recent trends. Anal Chim Acta 635(2):132–143
18. Reschiglian P, Moon MH (2008) Flow field-flow fractionation: a pre-analytical method for proteomics. J Proteome 71(3):265–276
19. Fraunhofer W, Winter G (2004) The use of asymmetrical flow field-flow fractionation in pharmaceutics and biopharmaceutics. Eur J Pharm Biopharm 58(2):369–383
20. Pasch H, Makan AC, Chirowodza H, Ngaza N, Hiller W (2013) Analysis of complex polymers by multidetector field-flow fractionation. Anal Bioanal Chem. doi:10.1007/s00213-013-7308-0
21. Bednar AJ, Poda AR, Mitrano DM, Kennedy AJ, Gray EP, Ranville JF, Hayes CA, Crocker FH, Steevens JA (2013) Comparison of on-line detectors for field flow fractionation analysis of nanomaterials. Talanta 104:140–148
22. Gigault J, Hackley VA (2013) Differentiation and characterization of isotopically modifier silver nanoparticles in aqueous media using asymmetric flow field flow fractionation coupled to optical detection and mass spectrometry. Anal Chim Acta 763:57–66
23. Hinterwith H, Wiedmer SK, Moilanen M, Lehner A, Allmaier G, Waitz T, Lindner W, Lämmerhofer M (2013) Comparative method evaluation for size and size-distribution analysis of gold nanoparticles. J Sep Sci 36:2952–2961
24. Loeschner K, Navratilova J, Legros S, Wagner S, Grombe R, Snell J, von der Krammer F, Larsen EH (2013) Optimization and evaluation of asymmetrical flow field-flow fractionation of silver nanoparticles. J Chromatogr A 1272:116–125
25. Runyon JR, Goering A, Yong K-T, Ratanathanawongs W (2013) Preparation of narrow dispersity gold nanorods by asymmetrical flow field flow fractionation and investigation of surface plasmon resonance. Anal Chem 85:940–948
26. Moon MH, Giddins JC (1993) Size distribution of liposomes by flow field-flow fractionation. J Pharm Biomed Anal 11:911–920
27. Jahn A, Vreeland WN, DeVoes DL, Locascio LE, Gaitan M (2007) Microfluidic directed formation of liposomes of controlled size. Langmuir 23:6289–6293
28. Kalucerovic GN, Dietrich A, Kommera H, Kuntsche J, Mäder K, Mueller T, Paschke R (2012) Liposomes as vehicles for water insoluble platinum-based potential drug: 2-(4-(tetrahydro-2H-pyran-2-yloxy)-undecyl)-propane-1,3-diamminedichloroplatinum(II). Eur J Med Chem 54:567–572
29. Kang DY, Kim MJ, Kim ST, Oh KS, Yuk SH, Lee S (2008) Size characterization of drug-loaded polymeric core/shell nanoparticles using asymmetrical flow field-flow fractionation. Anal Bioanal Chem 390:2183–2188
30. Kuntsche J, Decker C, Fahr A (2012) Analysis of liposomes using asymmetrical flow field-flow fractionation: separation conditions and drug/lipid recovery. J Sep Sci 35:1993–2001
31. Horie M, Kato H, Iwahashi H (2013) Cellular effects of manufactured nanoparticles: effect of adsorption ability of nanoparticles. Arch Toxicol. doi:10.1007/s00204-013-1033-5
32. Zillies JC, Zwiorek K, Winter G, Coester C (2007) Method for quantifying the PEGylation of gelatin nanoparticle drug carrier systems using asymmetrical flow field-flow fractionation and refractive index detection. Anal Chem 79:4574–4580
33. Schädlich A, Caysa H, Mueller T, Tenambergen F, Rose C, Göpferich A, Kuntsche J, Mäder K (2011) Tumor accumulation of NIR fluorescent PEG-PLA nanoparticles: impact of particle size and human xenograft tumor model. ACS Nano 5:8710–8720
34. Schädlich A, Rose C, Kuntsche J, Caysa H, Mueller T, Göpferich A, Mäder K (2011) How stealthy are PEG-PLA nanoparticles? An NIR in vivo study combined with detailed size measurements. Pharm Res 28(1995–2007)
35. Ehrhart J, Mingotaud A-F, Violleau F (2011) Asymmetrical flow field-flow fractionation with multi-angle light scattering and quasi elastic light scattering for characterization of poly(ethyleneglycol-b-ε-caprolactone) block copolymer self-assemblies used as drug carriers for photodynamic therapy. J Chromatogr A 1218: 4249–4256
36. Knop K, Mingotaud A-F, El-Akra N, Violleau F, Souchard J-P (2009) Monomeric pheophorbide(a)-containing poly(ethyleneglycol-b-ε-caprolactone)micelles for photodynamic therapy. Photochem Photobiol Sci 8:396–404
37. Miller T, Rachel R, Besheer A, Uezguen S, Weigandt M, Göpferich A (2012) Comparative investigations on in vitro serum stability of polymeric micelle formulations. Pharm Res 29:448–459
38. Brulet A, Lairez D, Lapp A, Cotton JP (2007) Improvement of data treatment in small-angle neutron scattering. J Appl Crystallogr 40: 165–177
39. Cotton JP (1991) In: Lindler P. Zemb T (eds) Neutron, x-ray and light scattering. North Holland, Amsterdam, p 19
40. Discher DE, Eisenberg A (2002) Polymer vesicles. Science 297: 967–973
41. Sachl R, Stepanek M, Prochazka K, HumpolicÌŒkova J, Hof M (2007) Fluorescence study of the solvation of fluorescent probes prodan and laurdan in poly(caprolactone)-block-poly(ethylene oxide) vesicles in aqueous solutions with tetrahydrofurane. Langmuir 24(1): 288–295
42. Sachl R, Uchman M, Matejicek P, Prochazka K, Stepanek M, Spirkova M (2007) Preparation and characterization of self-assembled nanoparticles formed by poly(ethylene oxide)-block-poly(Îμ-caprolactone) copolymers with long poly(caprolactone) blocks in aqueous solutions. Langmuir 23(6):3395–3400
43. Liu Y, Tan J, Thomas A, Ou-Yang D, Muzykantov VR (2012) The shape of things to come: importance of design in nanotechnology for drug delivery. Ther Deliv 3(2):181–194
44. Toy R, Hayden E, Shoup C, Baskaran H, Karathanasis E (2011) The effects of particle size, density and shape on margination of nanoparticles in microcirculation. Nanotechnology 22:115101
45. Gayet F, Marty J-D, Brulet A (2011) Vesicles in ionic liquids. Langmuir 27(16):9706–9710
46. Hocine S, Cui D, Rager M-N, Di Cicco A, Liu J-M, Wdzieczak-Bakala J, Brulet A (2013) Polymersomes with PEG corona: structural changes and controlled release induced by temperature variation. Langmuir 29(5):1356–1369
47. Salva R, Le Meins J-F, Sandre O, Brulet A, Schmutz M, Guenoun P, Lecommandoux S (2013) Polymersome shape transformation at the nanoscale. ACS Nano 7(10):9298–9311